Petroleum Science 21 (2024) 327–342

Contents lists available at ScienceDirect

Petroleum Science

journal homepage: www.keaipublishing.com/en/journals/petroleum-science

Original Paper

A semi-analytical model for coupled flow in stress-sensitive multi-scale shale reservoirs with fractal characteristics

Qian Zhang [a, b], Wen-Dong Wang [a, b, *], Yu-Liang Su [a, b], Wei Chen [c], Zheng-Dong Lei [d], Lei Li [a, b], Yong-Mao Hao [a, b]

[a] Key Laboratory of Unconventional Oil & Gas Development (China University of Petroleum (East China)), Ministry of Education, Qingdao, 266580, Shandong, China
[b] School of Petroleum Engineering, China University of Petroleum (East China), Qingdao, 266580, Shandong, China
[c] Shale Oil Development Branch, Changqing Oilfield Company, PetroChina, Qingyang, 745708, Gansu, China
[d] PetroChina Research Institute of Petroleum Exploration & Development, Beijing, 100083, China

ARTICLE INFO

Article history:
Received 30 May 2023
Received in revised form
26 September 2023
Accepted 1 October 2023
Available online 5 October 2023

Edited by Yan-Hua Sun

Keywords:
Multi-scale coupled flow
Stress sensitivity
Shale oil
Micro-scale effect
Fractal theory

ABSTRACT

A large number of nanopores and complex fracture structures in shale reservoirs results in multi-scale flow of oil. With the development of shale oil reservoirs, the permeability of multi-scale media undergoes changes due to stress sensitivity, which plays a crucial role in controlling pressure propagation and oil flow. This paper proposes a multi-scale coupled flow mathematical model of matrix nanopores, induced fractures, and hydraulic fractures. In this model, the micro-scale effects of shale oil flow in fractal nanopores, fractal induced fracture network, and stress sensitivity of multi-scale media are considered. We solved the model iteratively using Pedrosa transform, semi-analytic Segmented Bessel function, Laplace transform. The results of this model exhibit good agreement with the numerical solution and field production data, confirming the high accuracy of the model. As well, the influence of stress sensitivity on permeability, pressure and production is analyzed. It is shown that the permeability and production decrease significantly when induced fractures are weakly supported. Closed induced fractures can inhibit interporosity flow in the stimulated reservoir volume (SRV). It has been shown in sensitivity analysis that hydraulic fractures are beneficial to early production, and induced fractures in SRV are beneficial to middle production. The model can characterize multi-scale flow characteristics of shale oil, providing theoretical guidance for rapid productivity evaluation.

1. Introduction

Shale and tight oil reservoirs are reconstructed by massive hydraulic fracturing (Guo et al., 2021; Gonzalez et al., 2014). The reconstructed reservoir can be divided into four subsystems, including organic matter, inorganic matter, induced fractures and hydraulic fractures (Lei et al., 2023). Because different subsystems have different structures, their characteristics will influence well performance on different timescales (Zeng et al., 2021).

Ideal productivity is achieved through a complex fracture network that develops over the entire well interval. Although microseismic monitoring can be used to track and invert fracture network around hydraulic fractures in shale reservoirs, it is not yet mature enough to describe fracture network morphology directly (Yao et al., 2013; Li et al., 2019). As fracture morphology after fracturing has certain fractal characteristics, it is possible to characterize the induced fractures around hydraulic fractures using a fractal theory model (Li et al., 2018; Valdes-Perez and Blasingame, 2021). Wang et al. (2015) applied fractal theory to the dual-porosity media model, characterizing heterogeneous porosity and permeability of induced fractures in stimulated reservoir volume (SRV). Fan and Ettehadtavakkol (2017) established a transient flow model for fractured horizontal wells in shale gas reservoirs by considering the fractal distribution of induced fracture density, porosity, and permeability, and estimated the fractal parameters after fracturing combined with microseismic data. Sheng et al. (2019) developed a dual-fractal diffusion model for hydraulic fractured horizontal

* Corresponding author. Key Laboratory of Unconventional Oil & Gas Development (China University of Petroleum (East China)), Ministry of Education, Qingdao, 266580, Shandong, China.
E-mail address: wwdong@upc.edu.cn (W.-D. Wang).

https://doi.org/10.1016/j.petsci.2023.10.003

wells in shale gas reservoirs, considering the variation in shape factor of matrix blocks due to changes in induced fracture spacing.

However, it is typical for shale reservoirs to contain organic matter, and the pore characteristics of shale reservoirs are complex (for example, abundant nanopores, natural fractures, rich in organic matter, and different pore geometry) (Feng et al., 2019; Wang et al., 2022). Nanoscale pores are dominant, and strong solid–liquid interaction exists in confined space, which exacerbates the nonlinear characteristics of the flow (Wang et al., 2016; Zhang et al., 2023). Organic pores with diameter smaller than 2 nm exhibit a rapid decrease in apparent permeability (Zhang et al., 2018), and they have a smaller permeability and higher flow resistance than inorganic pores. The complex structure of shale nanopores greatly impacts oil and gas flow behavior and oil recovery (Zhang et al., 2019), traditional Darcy's law may not be able to describe shale oil transport. To characterize the transport mechanism in shale nanopores, Cui et al. (2017) proposed a flow-enhanced model to explain slip flow and physical adsorption in organic nanopores. Many scholars have established shale apparent permeability models by combining different transport mechanisms in inorganic and organic nanopores, considering adsorption, diffusion, slip, oil viscosity, pore structure and distribution, and other microscopic mechanisms (Zhang et al., 2017; Zeng et al., 2020; Zhu et al., 2020). These models provided an effective understanding of how oil and water transport within nanopores.

Nanopores transport mechanisms are complex, and tight reservoirs are also stress sensitive (Ren et al., 2017). Due to the high content of clay minerals in shale and the existence of a large number of nanopores and fractures, stress sensitivity is more likely to occur under the action of external forces (Yan et al., 2019). Especially, in the production process, fractures can gradually close with the production of oil and gas, which will not only lead to compaction, but also lead to proppant embedding and crushing (Luo et al., 2018; Zhang and Emami-Meybodi, 2020; Zheng et al., 2020). The shale permeability is highly stress-dependent (Bustin et al., 2008; Chen et al., 2015), ignoring the stress sensitivity of matrix permeability and fracture conductivity will overestimate production (Qanbari and Clarkson, 2013). Scholars have proposed a variety of mathematical models to quantitatively describe stress sensitivity (Bernabe, 1986; Pedrosa, 1986), the two most commonly used models to describe the stress sensitivity are power law equation and exponential equation, among which the exponential equation is the most widely used in shale (Chhatre et al., 2014; Yang et al., 2017).

The previous models for fractured horizontal wells do not consider the micro-scale effect and transport mechanism of shale oil. In addition, fluid behavior and transport properties in different media are also different (Cai et al., 2019), so they are not suitable for shale reservoirs dominated by nanopores and coexisting with multi-scale media. In this paper, a multi-scale coupled flow model is constructed by considering the heterogeneous distribution of induced fractures, the micro-scale effect of nanopores in the shale matrix and the stress-sensitive characteristics of multi-scale media. This study presents a comparative analysis of pressure and production in shale oil reservoirs exhibiting different stress sensitivity. Furthermore, we also compared the permeability loss in multi-scale media, as well as differences in the interporosity flow coefficient among shale reservoirs with different stress sensitivity. Finally, we conducted sensitivity analyses for hydraulic fracture and SRV parameters.

2. Mathematical model

2.1. Concept model

According to the flow characteristics of multi-stage fractured horizontal wells (Fig. 1(a)), the control area of single hydraulic fracture is divided into three zones (Fig. 1(b)). The first zone is the hydraulic fracture zone, the second zone is the SRV, and the third zone is the unstimulated reservoir volume (UNSRV). In order to capture the complex transport mechanism in the shale matrix, nanopores in the matrix system (Fig. 1(c)) are divided into organic and inorganic pores (Fig. 1(d)). As shown in the SEM images of shale samples, this model can also be applied to tight oil reservoirs without the organic matter.

In this paper, considering the micro-scale effects of shale and the stress sensitivity of multi-scale media, the coupled flow model of multi-stage fractured horizontal well in shale oil reservoir with box boundary and complex induced fracture network is established. The following assumptions are briefly described:

(1) A fractured horizontal well is in the center of a box reservoir with a closed outer boundary, the initial pressure and the thickness of the reservoir are constant.
(2) Organic and inorganic nanopores are arranged in parallel without considering fluid exchange between them.
(3) The induced fractures are spatially variable.
(4) Hydraulic fracture (HF) is the only channel connecting induced fractures and the wellbore.
(5) Under the same pore pressure, organic pores and inorganic pores have the same stress dependence. The stress sensitivity of induced fractures and hydraulic fractures is different.

2.2. Matrix model

2.2.1. Oil transport mechanisms in nanopores

To begin with, we first determine the mass flux of organic matter and inorganic matter, and further determine the apparent oil permeability in matrix as follows:

Assuming that the pore pressure and stress dependence of organic matter and inorganic matter are the same, according to the theory proposed by Pedrosa (1986), the stress-sensitive permeability of organic matter can be described as:

$$k_{\mathrm{im}} = k_{\mathrm{im,i}} \mathrm{e}^{-\gamma_{\mathrm{m}}(p_{\mathrm{i}} - p_{\mathrm{m}})}, \tag{1}$$

where $k_{\mathrm{im,i}}$ is the initial permeability of inorganic pores, D; γ_{m} is the stress sensitive coefficient of nanopores, MPa^{-1}; p_{i} is the initial reservoir pressure, MPa; p_{m} is the matrix pressure, MPa.

The mass flux and apparent permeability models are derived by using the water flow model in carbon nanotubes based on the steady-state HP (Hagen–Poiseuille) equation proposed by Mattia and Calabrò (2012).

$$k_{\mathrm{im,i}} = \frac{\phi_{\mathrm{im,i}} R_{\mathrm{im,i}}^2}{8\tau_{\mathrm{im,i}}}, \tag{2}$$

where $\phi_{\mathrm{im,i}}$ is the initial porosity of inorganic matter; $\tau_{\mathrm{im,i}}$ is the initial tortuosity of inorganic pore; $R_{\mathrm{im,i}}$ is the radius of initial inorganic pore, nm;

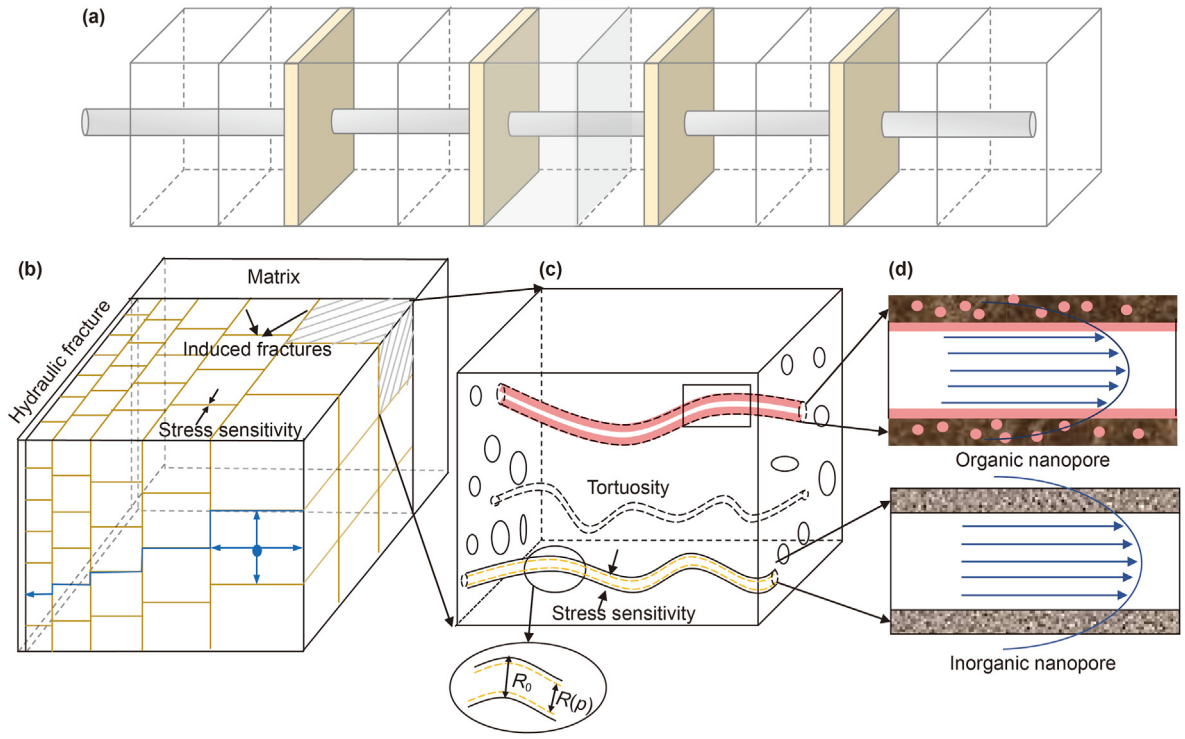

Fig. 1. Physical model for multi-stage fractured horizontal well. (**a**) Equivalent model of fractured horizontal well; (**b**) Matrix–fracture distribution in the quarter area controlled by the hydraulic fracture; (**c**) Schematic of matrix; (**d**) Oil transport through nanopores.

In real shale reservoirs, the pores show tortuous geometry, so it is necessary to consider the influence of tortuosity on oil flow in matrix. According to the fractal theory, there is a fractal relationship between the real length and characteristic length of an object (Yu and Cheng, 2002). For porous media, capillary diameter can be used as the characteristic length of an object (Hu et al., 2021).

$$\tau_{\mathrm{im}} = (2R_{\mathrm{im}})^{1-D_\tau} L_s^{D_\tau - 1}, \tag{3}$$

where D_τ is the fractal dimension of tortuosity in nanopores; L_s is the characteristic length, nm.

The radius of inorganic pore can be obtained by combining Eqs. (1)–(3).

$$R_{\mathrm{im}} = R_{\mathrm{im,i}} e^{\frac{1}{1+D_\tau}(-\gamma_{\mathrm{m}}+C_{\mathrm{m}})(p_{\mathrm{i}}-p_{\mathrm{m}})}. \tag{4}$$

The relationship between velocity distribution and pressure described by HP without velocity slip can be written:

$$v(r) = \frac{\partial p}{\partial x}\frac{R^2 - r^2}{4\mu}. \tag{5}$$

The slip boundary conditions of inorganic nanopores play a crucial role in the transport of liquid hydrocarbons (Zhang et al., 2017), velocity slip occurs on the pore wall. Moreover, clay minerals have large surfaces, enabling shale oil to adsorb on inorganic pores formed from them (Li et al., 2016). According to the boundary slip condition (Appendix A), the velocity distribution of bulk and near-wall region inside the inorganic nanopores can be obtained. On this basis, the total mass flux of inorganic matter in a single capillary can be expressed as:

$$J_{\mathrm{im}} = \pi\rho_{\mathrm{o}}\left[\frac{(R_{\mathrm{im}}-\delta_{\mathrm{im}})^2}{8}\left(\frac{(R_{\mathrm{im}}-\delta_{\mathrm{im}})^2}{\mu_{\mathrm{m}}} + \frac{4R_{\mathrm{im}}\delta_{\mathrm{im}} - 2\delta_{\mathrm{im}}^2 + 4\lambda_{\mathrm{im}}R_{\mathrm{im}}}{\mu_{\mathrm{im}}}\right) + \frac{2R_{\mathrm{im}}\delta_{\mathrm{im}} - \delta_{\mathrm{im}}{}^2}{8\mu_{\mathrm{im}}}\left(2R_{\mathrm{im}}\delta_{\mathrm{im}} - \delta_{\mathrm{im}}{}^2 + 4R_{\mathrm{im}}\lambda_{\mathrm{im}}\right)\right]\frac{\partial p_{\mathrm{m}}}{\partial x}. \tag{6}$$

Molecular structure differences between shale oil and hydrocarbon source rock are small, resulting in strong affinity between them, and shale oil can readily adsorb on organic pores (Wang et al., 2019). To accurately characterize fluid transport in organic pores, the adsorption layer thickness should be considered. Oil transport in organic pores, $\mu_{\mathrm{im}} = \infty$; $\lambda_{\mathrm{om}} = 0$, the mass flux of organic matter in a single capillary can be expressed as:

$$J_{\mathrm{om}} = \pi\rho_{\mathrm{o}}\frac{(R_{\mathrm{om}}-\delta_{\mathrm{om}})^4}{8\mu_{\mathrm{m}}}\frac{\partial p_{\mathrm{m}}}{\partial x}, \tag{7}$$

where C_{m} is the compressibility of the matrix, MPa^{-1}; δ_{im} is the thickness of the adsorption layer in the inorganic pore, nm; λ_{im} is the slip length in inorganic pore, nm; ρ_{o} is the oil density, $\mathrm{kg/m^3}$; μ_{im} is the viscosity of near-wall region inside the inorganic pore, mPa s; μ_{m} is the viscosity of bulk region in the inorganic pore, mPa s; δ_{om} is the thickness of the adsorption layer in the organic pore, nm.

By combining Eqs. (4)–(6), Darcy's law can be applied to calculate the permeability of inorganic matter under stress sensitivity influence:

$$k_{im}=\frac{\phi_{im,i}}{2^{1-D_\tau}L_s^{D_\tau-1}}\left[\begin{array}{l}\frac{R_{im,i}^{1+D_\tau}}{8}e^{-\gamma_m(p_i-p_m)}+\left(\frac{1}{8}-\frac{\mu_m}{8\mu_{im}}\right)\delta_{im}^4R_{im,i}^{-3+D_\tau}e^{\left(-C_m+\frac{-3+D_\tau}{1+D_\tau}(C_m-\gamma_m)\right)(p_i-p_m)}\\+\left(\frac{3}{4}-\frac{3\mu_m}{4\mu_{im}}\right)\delta_{im}^2R_{im,i}^{-1+D_\tau}e^{\left(-C_m+\frac{-1+D_\tau}{1+D_\tau}(C_m-\gamma_m)\right)(p_i-p_m)}+\left(-\frac{1}{2}+\frac{\mu_m}{2\mu_{im}}\right)R_{im,i}^{-2+D_\tau}\delta_{im}^3e^{\left(-C_m+\frac{-2+D_\tau}{1+D_\tau}(C_m-\gamma_m)\right)(p_i-p_m)}\\+\left(-\frac{\delta_{im}}{2}+\frac{\mu_m(\delta_{im}+\lambda_{im})}{2\mu_{im}}\right)R_{im,i}^{D_\tau}e^{\left(-C_m+\frac{D_\tau}{1+D_\tau}(C_m-\gamma_m)\right)(p_i-p_m)}\end{array}\right]. \tag{8}$$

Permeability of organic matter:

$$k_{om}=\frac{\phi_{om,i}}{2^{1-D_\tau}L_s^{D_\tau-1}}\times\left[\frac{R_{om,i}^{1+D_\tau}e^{-\gamma_m(p_i-p_m)}+\delta_{om}^4R_{om,i}^{-3+D_\tau}e^{\left(-C_m+\frac{-3+D_\tau}{D_\tau+1}(C_m-\gamma_m)\right)(p_i-p_m)}-4R_{om,i}^{-2+D_\tau}\delta_{im}^3e^{\left(-C_m+\frac{-2+D_\tau}{D_\tau+1}(C_m-\gamma_m)\right)(p_i-p_m)}-4R_{om,i}^{D_\tau}\delta_{om}e^{\left(-C_m+\frac{D_\tau}{D_\tau+1}(C_m-\gamma_m)\right)(p_i-p_m)}+6\delta_{om}^2R_{om,i}^{-1+D_\tau}e^{\left(-C_m+\frac{-1+D_\tau}{D_\tau+1}(C_m-\gamma_m)\right)(p_i-p_m)}}{8}\right], \tag{9}$$

where μ_{om} is the viscosity of near-wall in the organic pore, mPa s; $\phi_{om,i}$ is the initial porosity of organic matter; $\tau_{om,i}$ is the tortuosity of the inorganic pore; $R_{om,i}$ is the initial radius of the organic pore, nm.

Based on the hypothesis that organic pores and inorganic pores are arranged in parallel, the volume fraction of organic matter φ is introduced to obtain the total apparent permeability of liquid (Yu et al., 2018).

$$k_m=\frac{1}{2^{1-D_\tau}L_s^{D_\tau-1}}\left(b_1e^{-a_1(p_i-p_m)}+b_2e^{-a_2(p_i-p_m)}+b_3e^{-a_3(p_i-p_m)}+b_4e^{-a_4(p_i-p_m)}+b_5e^{-a_5(p_i-p_m)}\right), \tag{10}$$

with

$$a_1=\gamma_m,$$

$$a_2=C_m-\frac{D_\tau}{D_\tau+1}(C_m-\gamma_m),$$

$$a_3=C_m-\frac{-1+D_\tau}{D_\tau+1}(C_m-\gamma_m),$$

$$a_4=C_m-\frac{-2+D_\tau}{D_\tau+1}(C_m-\gamma_m),$$

$$a_5=C_m-\frac{-3+D_\tau}{D_\tau+1}(C_m-\gamma_m),$$

$$b_1=\frac{(1-\varphi)R_{im,i}^{1+D_\tau}\phi_{im,i}+\varphi R_{om,i}^{1+D_\tau}\phi_{om,i}}{8},$$

$$b_2=(1-\varphi)\left(-\frac{\delta_{im}}{2}+\frac{\mu_m(\delta_{im}+\lambda_{im})}{2\mu_{im}}\right)R_{im,i}^{D_\tau}\phi_{im,i}-\frac{\varphi R_{om,i}^{D_\tau}\phi_{om,i}}{2},$$

$$b_3=(1-\varphi)\left(\frac{3}{4}-\frac{3\mu_m}{4\mu_{im}}\right)\delta_{im}^2R_{im,i}^{-1+D_\tau}\phi_{im,i}+\frac{3\varphi\delta_{om}^2R_{om,i}^{-1+D_\tau}\phi_{om,i}}{4},$$

$$b_4=(1-\varphi)\left(-\frac{1}{2}+\frac{\mu_m}{2\mu_{im}}\right)R_{im,i}^{-2+D_\tau}\delta_{im}^3\phi_{im,i}-\varphi\frac{R_{om,i}^{-2+D_\tau}\delta_{om}^3}{2}\phi_{om,i},$$

$$b_5=(1-\varphi)\left(\frac{1}{8}-\frac{\mu_m}{8\mu_{im}}\right)\delta_{im}^4R_{im,i}^{-3+D_\tau}\phi_{im,i}+\frac{\varphi\delta_{om}^4R_{om,i}^{-3+D_\tau}\phi_{om,i}}{8}.$$

2.2.2. Flow model in UNSRV

Based on the above apparent permeability model, the flow model in the matrix was established:

$$\frac{1}{2^{1-D_\tau}L_s^{D_\tau-1}}\left[-M_{3a}\left(\frac{\partial p_{3m}}{\partial x}\right)^2+M_{3m}\frac{\partial^2 p_{3m}}{\partial x^2}\right]=\mu_m\phi_m C_{tm}\frac{\partial p_{3m}}{\partial t}, \tag{11}$$

with

$$M_{3m}=b_1e^{-a_1(p_i-p_{3m})}+b_2e^{-a_2(p_i-p_{3m})}+b_3e^{-a_3(p_i-p_{3m})}+b_4e^{-a_4(p_i-p_{3m})}+b_5e^{-a_5(p_i-p_{3m})},$$

$$M_{3a}=a_1b_1e^{-a_1(p_i-p_{3m})}+a_2b_2e^{-a_2(p_i-p_{3m})}+a_3b_3e^{-a_3(p_i-p_{3m})}+a_4b_4e^{-a_4(p_i-p_{3m})}+a_5b_5e^{-a_5(p_i-p_{3m})}.$$

The following equation can be obtained by substituting the dimensionless variables into Eq. (11).

$$-\chi_{3D}\left(\frac{\partial p_{3mD}}{\partial x_D}\right)^2+\frac{\partial^2 p_{3mD}}{\partial x_D^2}=\frac{2^{1-D}L_s^{D-1}k_w}{M_{3m}}\frac{\partial p_{3mD}}{\partial t_D}, \tag{12}$$

where k_w is the reference point permeability of induced fractures, D; $\chi_{3D}=\frac{M_{3aD}}{M_{3mD}}$ is much less than 0. The following flow equation is obtained by Perturbation transform (Appendix B) and Laplace transform.

$$\begin{cases}\dfrac{\partial^2\overline{\xi_{3mD}}}{\partial x_D^2}=F_3s\overline{\xi_{3mD}}\\ \overline{\xi_{3mD}}|_{x_D=1}=\overline{\xi_{fD}}|_{x_D=1}\\ \dfrac{\overline{\xi_{3mD}}}{\partial x_D}|_{x_D=x_{eD}}=0\end{cases}, \tag{13}$$

with

$$F_3=\frac{2^{1-D_\tau}L_s^{D_\tau-1}k_w}{M_{3m}}.$$

Pressure (Eq. (14)) and pressure derivative (Eq. (15)) in UNSRV are as follows:

$$\overline{\xi_{3mD}}=\frac{\exp\left(-2\sqrt{F_3s}x_{eD}+\sqrt{F_3s}x_D\right)+\exp\left(-\sqrt{F_3s}x_D\right)}{\exp\left(-2\sqrt{F_3s}x_{eD}+\sqrt{F_3s}\right)+\exp\left(-\sqrt{F_3s}\right)}\overline{\xi_{fD}}|_{x_D=1}, \tag{14}$$

$$\frac{\overline{\xi_{3mD}}}{\partial x_D}\Big|_{x_D=1}=\sqrt{F_3s}\tanh\left(-\sqrt{F_3s}x_{eD}+\sqrt{F_3s}\right)\overline{\xi_{fD}}|_{x_D=1}. \tag{15}$$

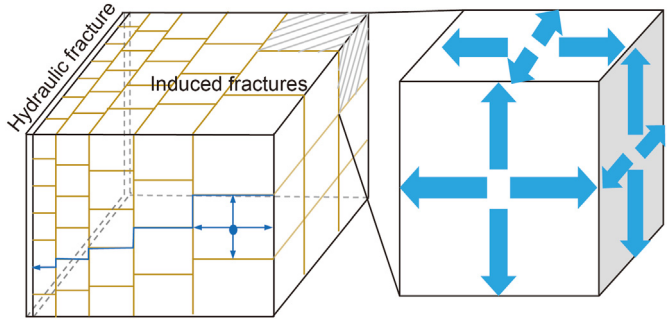

Fig. 2. Induced fracture distribution and oil flow within matrix block.

2.3. Induced fracture model

Shale reservoirs typically develop natural fractures, and the stress undergoes changes over time. As a result, it is easy to form complex fracture networks during fracturing (Nandlal and Weijermars, 2019). Fractal geometry has been widely used to characterize complex fracture network. Al-Obaidy et al. (2014) create a branching fractal model to capture the complexity of the fracture network.

In general, fluid transfer between matrix and fracture is characterized by a dual-porosity media model (Ding, 2019). In dual-porosity media model, the flow of fluid can be classified into transient state flow (Kazemi, 1969) and pseudo-steady state flow (Warren and Root, 1963). Shape factor is a key parameter for analyzing interporosity flow in dual-porosity media model and represents the mass transfer capability between matrix and fracture (Mei et al., 2020). It is still rare, however, for fractal geometry to be applied to transfer function or shape factor. This paper is based on fractal theory to characterize the varying sizes of the matrix blocks and to modify the shape factor. Using fractal theory, we characterize induced fracture spacing (Sheng et al., 2019).

$$s_{fi}(y)=s_w\left(\frac{y}{w_f}\right)^{2-D_f}. \tag{16}$$

From Fig. 2, it can be observed that the spacing between induced fractures is equal to the size of the matrix blocks. The modified shape factor is as follows:

$$\alpha(y)=\frac{12}{{s_w}^2}\left(\frac{y}{w_f}\right)^{2-4D_f}, \tag{17}$$

where s_w is the fracture spacing at reference point, m; w_f is the half the width of the hydraulic fracture, m; D_f is the fractal dimension of induced fracture spacing.

We use fractal relations to account for permeability and porosity of induced fractures in shale oil reservoirs. The fractal permeability and porosity in the direction perpendicular to the hydraulic fracture are given as follows:

$$k_f(y)=k_w\left(\frac{y}{w_f}\right)^{D-2-\theta}e^{-\gamma_f(p_i-p_f)}, \tag{18}$$

$$\phi_f(y)=\phi_w\left(\frac{y}{w_f}\right)^{D-2}e^{-C_f(p_i-p_f)}, \tag{19}$$

where ϕ_w is the porosity of induced fracture at reference point; D is the fractal dimension of porosity and permeability; θ is the fractal index; γ_f is the stress sensitive coefficient of induced fractures, MPa^{-1}; C_f is the compressibility for induced fractures, MPa^{-1}.

The interporosity flow coefficient λ and ratio of storage capacity ω can characterize the flow capability from matrix to fractures. By considering the fractal characteristics and stress sensitivity of the matrix and induced fractures, modified expressions for these parameters can be obtained as follows:

$$\lambda(y)=\frac{12M_{2m}}{2^{1-D_\tau}L_s^{D_\tau-1}s_w^2k_we^{-\gamma_f(p_i-p_f)}}x_f^2\left(\frac{y}{w_f}\right)^{2D_f+\theta-D-2}, \tag{20}$$

$$\omega(y)=\frac{\phi_w C_{tf}}{\phi_m C_{tm}}\left(\frac{y}{w_f}\right)^{D-2}e^{-C_f(p_i-p_f)}, \tag{21}$$

where x_f is the half length of the hydraulic fracture, m.

Based on the fractal characteristics of the matrix and induced fractures mentioned above, we develop a pseudo-steady flow equation.

$$\frac{\partial p_{2mD}}{\partial t_D}=\alpha(y)\frac{M_{2m}}{2^{1-D_\tau}L_s^{D_\tau-1}k_w}x_f^2\left(p_{2mD}-p_{fD}\right). \tag{22}$$

The transient flow equation in the matrix is given below.

$$\frac{1}{2^{1-D_\tau}L_s^{D_\tau-1}}\left[M_{2m}\frac{\partial^2 p_{2m}}{\partial y'^2}-M_{2a}\left(\frac{\partial p_{2m}}{\partial y'}\right)^2\right]=\phi_m C_{tm}\frac{\partial p_{2m}}{\partial t}, \tag{23}$$

with

$$M_{2a}=a_1b_1e^{-a_1(p_i-p_{2m})}+a_2b_2e^{-a_2(p_i-p_{2m})}+a_3b_3e^{-a_3(p_i-p_{2m})}+a_4b_4e^{-a_4(p_i-p_{2m})}+a_5b_5e^{-a_5(p_i-p_{2m})},$$

$$M_{2m}=\left(b_1e^{-a_1(p_i-p_{2m})}+b_2e^{-a_2(p_i-p_{2m})}+b_3e^{-a_3(p_i-p_{2m})}+b_4e^{-a_4(p_i-p_{2m})}+b_5e^{-a_5(p_i-p_{2m})}\right).$$

In combination with dimensionless variables, Eq. (23) can be transformed into the following form:

$$\frac{\partial^2 p_{2mD}}{\partial y_D'^2}-\chi_{2D}\left(\frac{\partial p_{2mD}}{\partial y_D'}\right)^2=\frac{k_w}{M_{2m}}\frac{L_s^{D_\tau-1}}{2^{D_\tau-1}}\frac{\left(s_{fi}(y)\right)^2}{2^2}\frac{1}{x_f^2}\frac{\partial p_{2mD}}{\partial t_D}. \tag{24}$$

The following flow equation of matrix in SRV is obtained by Pedrosa transform, Perturbation transform and Laplace transform

$$\begin{cases}\dfrac{\partial^2\overline{\xi_{2mD}}}{\partial y_D'^2}=F_{2m}s\overline{\xi_{2mD}}\\ \left.\dfrac{\partial\overline{\xi_{2mD}}}{\partial y_D'}\right|_{y_D'=0}=0\\ \overline{\xi_{2mD}}|_{y_D'=1}=\left.\overline{\xi_{fD}}\right|_{y_D'=1}\end{cases}, \tag{25}$$

with

$$\chi_{2D}=\frac{M_{2aD}}{M_{2mD}},$$

$$F_{2m}=\frac{k_w}{M_{2m}}\frac{L_s^{D_\tau-1}}{2^{D_\tau-1}}\frac{\left(s_{fi}(y)\right)^2}{2^2}\frac{1}{x_f^2}.$$

Dimensionless pressure (Eq. (26)) and dimensionless pressure derivative (Eq. (27)) at matrix block boundary are shown below:

$$\overline{\xi_{2mD}}=\frac{\left(\exp\left(\sqrt{F_{2m}s}\,y_D'\right)+\exp\left(-\sqrt{F_{2m}s}\,y_D'\right)\right)\left.\overline{\xi_{fD}}\right|_{y_D'=1}}{\exp\left(\sqrt{F_{2m}s}\right)+\exp\left(-\sqrt{F_{2m}s}\right)}, \tag{26}$$

$$\left.\frac{\partial\overline{\xi_{2mD}}}{\partial y_D'}\right|_{y_D'=1}=\sqrt{F_{2m}s}\tanh\left(\sqrt{F_{2m}s}\right)\left.\overline{\xi_{fD}}\right|_{y_D'=1}. \tag{27}$$

The flow equation of induced fractures is established as follows:

$$\begin{aligned}&\frac{(D-2-\theta)}{y}e^{-\gamma_f(p_i-p_f)}\frac{\partial p_f}{\partial y}-\gamma_f e^{-\gamma_f(p_i-p_f)}\left(\frac{\partial p_f}{\partial y}\right)^2+e^{-\gamma_f(p_i-p_f)}\frac{\partial^2 p_f}{\partial y^2}\\ &\left.-\frac{2M_{2m}}{s_{fi}(y)k_w\left(\frac{y}{w_f}\right)^{D-2-\theta}2^{1-D_\tau}L_s^{D_\tau-1}}\frac{\partial p_m}{\partial y'}\right|_{y'=\frac{s_{fi}(y)}{2}}\\ &\left.+\frac{M_{3m}}{k_w\left(\frac{y}{w_f}\right)^{D-2-\theta}2^{1-D_\tau}L_s^{D_\tau-1}x_f}\frac{\partial p_3}{\partial x}\right|_{x=x_f}\\ &=\frac{\phi_w\left(\frac{y}{w_f}\right)^{\theta}C_{tf}e^{-C_f(p_i-p_f)}}{k_w}\frac{\partial p_f}{\partial t}.\end{aligned} \tag{28}$$

The mathematical model of the induced fracture can be obtained by dimensionless transformation, Pedrosa transformation, Perturbation transformation, and Laplace transformation.

$$\begin{cases}\dfrac{\partial^2\overline{\xi_{fD}}}{\partial y_D^2}+\dfrac{(D-2-\theta)}{y_D}\dfrac{\partial\overline{\xi_{fD}}}{\partial y_D}=\left(\dfrac{y}{w_f}\right)^{\theta}N(p,y_D)s\overline{\xi_{f_D}}\\ \left.\overline{\xi_{fD}}\right|_{y_D=\frac{w_{fD}}{2}}=\left.\overline{\xi_{1D}}\right|_{y_D=\frac{w_{fD}}{2}}\\ \left.\dfrac{\partial\overline{\xi_{fD}}}{\partial y_D}\right|_{y_D=y_{eD}}=0\end{cases}. \tag{29}$$

Transient state characteristic equation is as follows:

$$N(p,y_D)=\frac{2x_f}{s_{fi}(y)}\sqrt{\frac{M_{2m}2^{D_\tau-1}}{sk_wL_s^{D_\tau-1}}}\left(\frac{y}{w_f}\right)^{2-D}\tanh\left(\sqrt{\frac{sk_w}{M_{2m}}\frac{L_s^{D_\tau-1}}{2^{D_\tau-1}}}\frac{\left(s_{fi}(y)\right)}{2x_f}\right)-\sqrt{\frac{M_{3m}2^{D_\tau-1}}{sk_wL_s^{D_\tau-1}}}\tanh\left(\sqrt{s\frac{L_s^{D_\tau-1}k_w}{2^{D_\tau-1}M_{3m}}}-\sqrt{s\frac{L_s^{D_\tau-1}k_w}{2^{D_\tau-1}M_{3m}}}x_{eD}\right)\left(\frac{y}{w_f}\right)^{2-D}+\frac{\phi_w C_{tf}}{(\phi C_t)_m}$$

Pseudo-steady characteristic equation is as follows:

$$N(p,y_D)=\frac{12\frac{M_{2m}2^{D_\tau-1}}{L_s^{D_\tau-1}}x_f^2}{12\left(\frac{y}{w_f}\right)^{D-2}\frac{M_{2m}2^{D_\tau-1}}{L_s^{D_\tau-1}}x_f^2+s_w^2\left(\frac{y}{w_f}\right)^{4-2D_f}k_w s\left(\frac{y}{w_f}\right)^{D-2}}-\sqrt{\frac{M_{3m}2^{D_\tau-1}}{sk_wL_s^{D_\tau-1}}}\tanh\left(\sqrt{s\frac{L_s^{D_\tau-1}k_w}{2^{D_\tau-1}M_{3m}}}-\sqrt{s\frac{L_s^{D_\tau-1}k_w}{2^{D_\tau-1}M_{3m}}}x_{eD}\right)\left(\frac{y}{w_f}\right)^{2-D}+\frac{\phi_w C_{tf}}{(\phi C_t)_m}\Bigg).$$

The above equation has strong nonlinearity and is solved piecewise by Bessel function, SRV is divided into X segments with two outer boundaries and $X-1$ inner boundaries in the direction perpendicular to the hydraulic fracture.

$$\begin{aligned}&\frac{\partial^2\overline{\xi_{fDj}}}{\partial y_D^2}+\frac{(D-2-\theta)}{y_D}\frac{\partial\overline{\xi_{fDj}}}{\partial y_D}=\frac{b_j^+ + b_j^-}{2w_{fD}^{\theta}}y_D^{\theta}\overline{\xi_{fD}}\\&\left.\frac{\partial\overline{\xi_{fDj}}}{\partial y_D}\right|_{y_D=y_{jD}^-}=\overline{\xi_{fDj}}^{-'}\\&\left.\frac{\partial\overline{\xi_{fDj}}}{\partial y_D}\right|_{y_D=y_{jD}^+}=\overline{\xi_{fDj}}^{+'}\end{aligned}\quad(30)$$

Subsequently, solution for the induced fractures can be obtained by integrating flow equation with the boundary conditions, segment j can be written as follows, and Appendix C shows the detailed procedure.

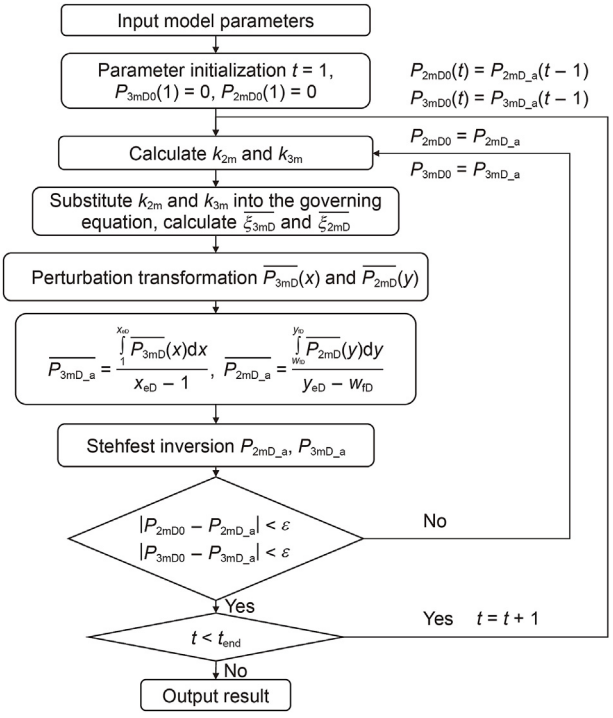

Fig. 3. The flowchart to obtain transient pressure of fractured horizontal well with a complex fracture network.

$$\begin{aligned}\overline{\xi_{fDj}}=\overline{\xi_{fDj}}^{-'}&\left(\frac{y_D^{\frac{1-h}{2}}}{\sqrt{B_j}\left(y_{jD}^-\right)^{\frac{1+g-2h}{2}}}\frac{I_j(y_D)K_j'\left(y_{jD}^+\right)+I_j'\left(y_{jD}^+\right)K_j(y_D)}{I_j'\left(y_{jD}^-\right)K_j'\left(y_{jD}^+\right)-I_j'\left(y_{jD}^+\right)K_j'\left(y_{jD}^-\right)}\right)\\&-\overline{\xi_{fDj}}^{+'}\left(\frac{y_D^{\frac{1-h}{2}}}{\sqrt{B_j}\left(y_{jD}^+\right)^{\frac{1+g-2h}{2}}}\frac{I_j(y_D)K_j'\left(y_{jD}^-\right)+I_j'\left(y_{jD}^-\right)K_j(y_D)}{I_j'\left(y_{jD}^-\right)K_j'\left(y_{jD}^+\right)-I_j'\left(y_{jD}^+\right)K_j'\left(y_{jD}^-\right)}\right),\end{aligned}\quad(31)$$

with

$$g=D-2,$$

$$h=D-2-\theta.$$

2.4. Hydraulic fracture model

Hydraulic fracture is the main flow channel, and the basic flow equation considering stress sensitivity is as follow:

$$-\gamma_1 k_{10}e^{-\gamma_1(p_i-p_1)}\left(\frac{\partial p_1}{\partial y}\right)^2+k_{10}e^{-\gamma_1(p_i-p_1)}\frac{\partial^2 p_1}{\partial x^2}+\frac{k_f}{w_f}\left.\frac{\partial p_f}{\partial x}\right|_{x=w_f}=\mu\phi_1 C_{t1}\frac{\partial p_1}{\partial t}\quad(32)$$

where γ_1 is the stress sensitive coefficient of hydraulic fracture, MPa^{-1}; k_{10} is the initial permeability of hydraulic fracture, D; ϕ_1 is the porosity of hydraulic fracture; C_{t1} is the compressibility for hydraulic fracture, MPa^{-1}.

The mathematical model of the hydraulic fracture can be obtained by dimensionless transformation, Pedrosa transformation, Perturbation transformation, and Laplace transformation:

$$\begin{cases}\dfrac{\partial^2\overline{\xi_{1D}}}{\partial x_D^2}=\left(\dfrac{\phi C_{t1}}{(\phi C_t)_m}\dfrac{k_w}{k_{10}}s-\dfrac{k_w x_f}{k_{10}w_f}F_2\right)\overline{\xi_{1D}}\\ \left.\dfrac{\partial\overline{\xi_{1D}}}{\partial x_D}\right|_{x_D=1}=0\\ \left.\dfrac{\partial\overline{\xi_{1D}}}{\partial x_D}\right|_{x_D=0}=-\dfrac{\overline{q_D}}{2}\dfrac{k_w x_f}{k_{10}w_f}\end{cases}.\quad(33)$$

Combined with the boundary conditions, the dimensionless bottom-hole pressure is obtained:

$$\overline{\xi_{1D}}=\frac{(1-e^{-\gamma_{1D}})\left(e^{\sqrt{F_1}(x_D-1)}+e^{-\sqrt{F_1}(x_D-1)}\right)}{s\gamma_{1D}\left(e^{\sqrt{F_1}}+e^{-\sqrt{F_1}}\right)},\quad(34)$$

with

$$F_1=\frac{\phi_1 C_{t1}}{(\phi C_t)_m}\frac{k_w}{k_{10}}s-\frac{k_w x_f}{k_{10}w_f}F_2.$$

Fig. 3 shows the iterative calculation process for multi-scale coupled flow model.

The workflow for calculating pressure and production at different times can be divided into 7 specific steps as follows:

(1) Specify initial values for the pressure of the matrix in SRV and UNSRV.

Table 1
Summary of parameters.

Parameter	Value
Thickness of adsorbed oil, nm	0.96
Slip length, nm	100
Inorganic pore size, nm	22.33
Organic pore size, nm	82.062
Initial porosity of organic matter	0.0184
Initial porosity of inorganic matter	0.0335
Oil viscosity ratio in inorganic nanopore	0.9
Oil viscosity ratio in organic nanopore	1.1
Total organic content	0.0467
Hydraulic fracture half-length, m	90.7
Hydraulic fracture width, m	0.0015
Permeability of induced fractures at the reference point, D	0.00179
Porosity of induced fractures at the reference point	7.1×10^{-4}
Induced fracture spacing at the reference point, m	0.17
Number of fractures	57
Initial pressure, MPa	48.6
Thickness, m	46

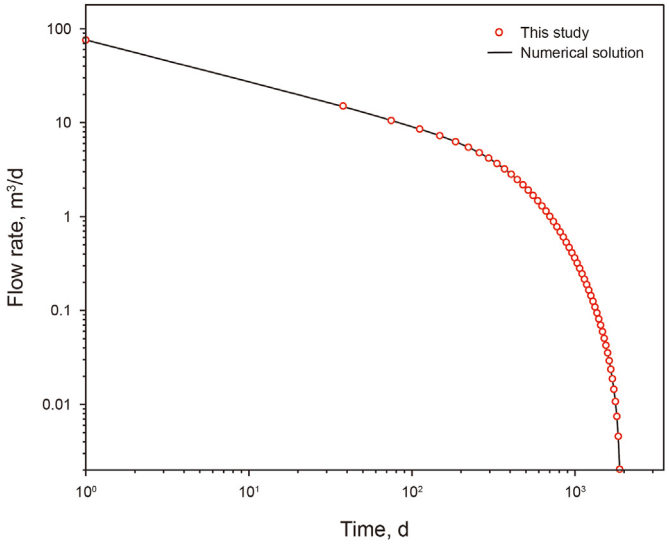

Fig. 4. Comparison between flow rate calculated by the model and the COMSOL numerical solution.

(2) Calculate the initial permeability of matrix in SRV and UNSRV according to Eq. (10).
(3) The pressure $\overline{\xi_{1D}}$, $\overline{\xi_{fD}}$ can be obtained by combining governing Eq. (15), Eq. (27) of matrix in SRV, the induced fracture in UNSRV and hydraulic fracture with Eq. (31) and Eq. (34), then the pressure $\overline{\xi_{2mD}}$ of matrix in SRV and the pressure $\overline{\xi_{3mD}}$ of matrix in UNSRV are obtained.
(4) The matrix pressure $\overline{p_{2mD}}$, $\overline{p_{3mD}}$ of SRV and UNSRV in Laplace space domain is obtained by Pedrosa transform and Perturbation transform, and then the average dimensionless pressure $\overline{p_{3mD\_a}}$, $\overline{p_{2mD\_a}}$ is obtained
(5) The average matrix pressure p_{3mD_a}, p_{2mD_a} of real spatial in SRV and UNSRV is obtained by Stehfest inversion and compared with the initial value.
(6) Stop the iteration if $|p_{3mD0}-p_{3mD\_a}|<\varepsilon$ and $|p_{2mD0}-p_{2mD\_a}|<\varepsilon$, and the pressure of this time step as the initial value of the next time step.
(7) Proceed to the next step and repeat steps (2)–(6) until the maximum test time is reached.

3. Results and discussion

The model was validated for accuracy by using numerical solution and production data from actual field. Furthermore, the analysis of pressure, production, and key parameters for reservoirs with varying stress sensitivity was conducted. And finally, hydraulic fracture and induced fracture parameters are analyzed for sensitivity.

3.1. Model validation

The proposed model in this study is compared with the numerical solution and actual production data obtained from the Cangdong shale reservoir. Table 1 presents the reservoir parameters used in this section.

The result obtained from numerical simulation using COMSOL and that from the semi-analytical model can be seen in Fig. 4 when the bottom-hole flow pressure is 10 MPa and remains unchanged. A good agreement exists between the semi-analytical and numerical solution for the flow rate, the calculation time of semi-analytical model is only 5 s, but the numerical solution of COMSOL takes 5 min.

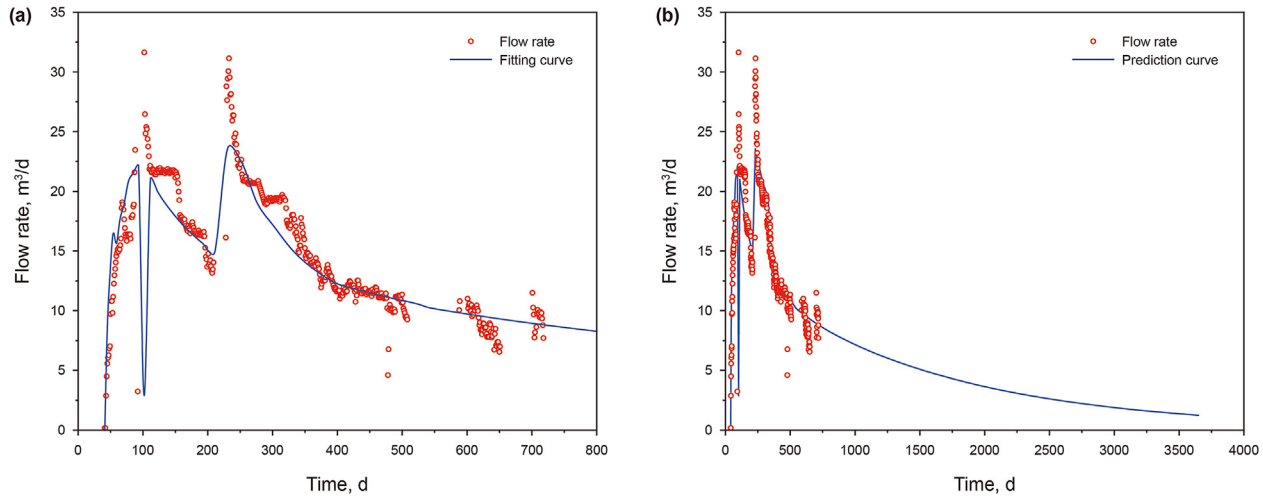

Fig. 5. Fitting and prediction of flow rate. (**a**) Fitting curve; (**b**) Prediction curve.

Table 2
A comparison of stress sensitive characteristics.

Case	Applicable case	Compressibility and stress sensitive coefficient, MPa^{-1}					
		C_{tm}	C_{tf}	C_{t1}	γ_m	γ_f	γ_1
Nanopores have much smaller compressibility and stress sensitivity than induced fractures. In addition, induced fractures have compressibility and stress sensitivity equal to hydraulic fractures	Proppant enters and supports the hydraulic fracture to compensate permeability loss due to stress sensitivity (Katende et al., 2023), and the proppant support is weak for the induced fractures.	6.61E-5	4.66E-4	4.66E-4	1.47E-4	4.66E-3	4.66E-3
Nanopores have compressibility and stress sensitivity equal to induced fractures. In addition, induced fractures have much smaller compressibility and stress sensitivity than hydraulic fractures	As well as hydraulic fractures, proppant enters induced fractures. As a result of proppant support, the partial loss of permeability in hydraulic fracture and induced fractures is compensated.	1.32E-4	1.32E-4	4.66E-4	1.18E-3	1.18E-3	4.66E-3

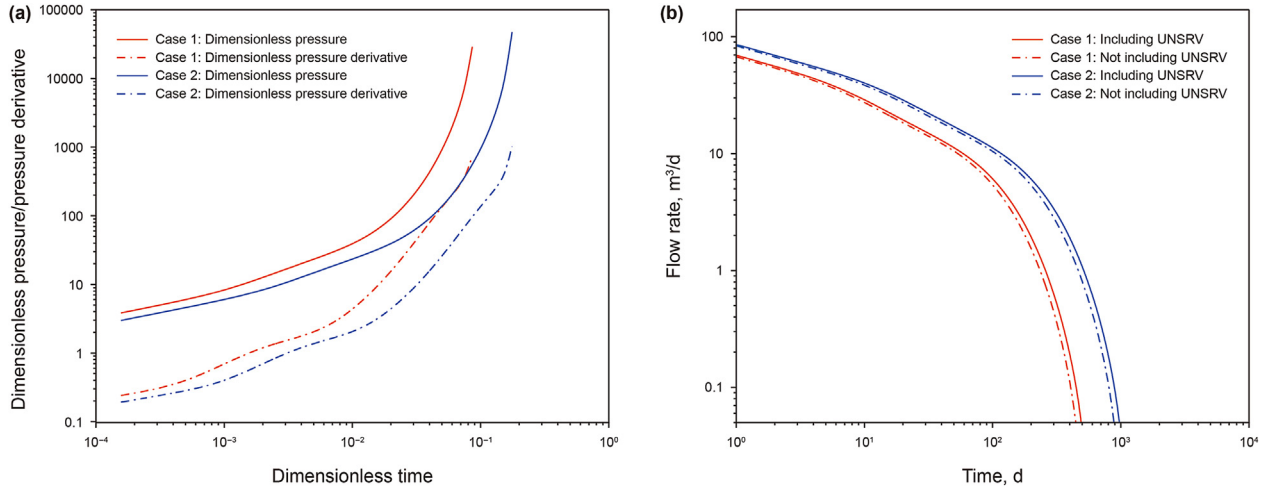

Fig. 6. Comparison of pressure and flow rate in two cases. (**a**) Pressure and pressure derivative; (**b**) Flow rate.

Based on the bottom-hole pressure from the field, we attempted to match the actual flow rate. The historical matching depicted in Fig. 5(a) demonstrates good consistency, confirming the accuracy of the proposed model. Furthermore, Fig. 5(b) illustrates the forecasting production of the model.

3.2. Analysis of stress sensitive characteristics

Stress significantly influences the permeability of both the shale matrix and fracture (Yang et al., 2019), with a greater impact observed on the permeability of fractured shale compared to intact shale (Gutierrez et al., 2015). In this section we consider the support strength of proppant in induced fractures, and analyze pressure, production and key parameters with two stress-sensitive characteristics. Compressibility and stress sensitive coefficient are shown in Table 2.

Fig. 6(a) shows that the dimensionless pressure derivative and dimensionless pressure are significantly larger in case 1 than in case 2. For case 1, the difference between dimensionless pressure and dimensionless pressure derivative grows significantly when $t_D > 0.04$, and it is clearly larger than in case 2. As can be seen in Fig. 6(b), the flow rate in case 1 is significantly lower than that in case 2. Early production differences between the two are relatively large, but the difference continues to decrease as the time increases. However, in both cases, the oil production from UNSRV is very small (Fig. 6(b)).

Different media are analyzed here in terms of their permeability loss. Fig. 7 illustrates the permeability ratio in different media. The matrix permeability ratio, for instance, is the ratio between the matrix permeability at any time and its initial permeability. The smaller the ratio, the more severe the permeability loss. Fig. 7(a) shows that the matrix permeability loss can reach 8% in case 1, but less than 2% in case 2. The UNSRV matrix permeability loss in both cases is less than the SRV matrix permeability loss. It is noted, however, that compared to case 2 the SRV matrix permeability loss in case 1 in the early stages is much higher than the UNSRV matrix permeability loss. The difference in permeability loss between the SRV and UNSRV in the two cases becomes smaller with production. The matrix permeability loss rate barely changes when $t > 500$ d in both cases.

Fig. 7(b) shows that hydraulic fractures can lose permeability more than 80% with production in both cases. Nevertheless, the permeability loss in case 1 is significantly faster than that in case 2.

Fig. 7(c) illustrates that, in the early stages of production, the closer the induced fracture is to the hydraulic fracture, the more significant the permeability loss is. Gradually, the difference in permeability loss of induced fractures at different location decreases. Induced fractures in case 1 exhibit much greater permeability loss than in case 2. The permeability of the induced fractures in case 2 declines by about 30% with production.

From Fig. 7(d), we can see that the permeability loss increases when the distance gets closer and closer, when $y_f > 4$ m, as the distance increases, induced fractures show a smaller change in permeability loss. In case 1, the permeability loss near the hydraulic fracture is more than 10%, while in case 2, the permeability loss is only about 3%.

In both cases, hydraulic fractures have the same compressibility and stress sensitive coefficient. The stress sensitivity of induced

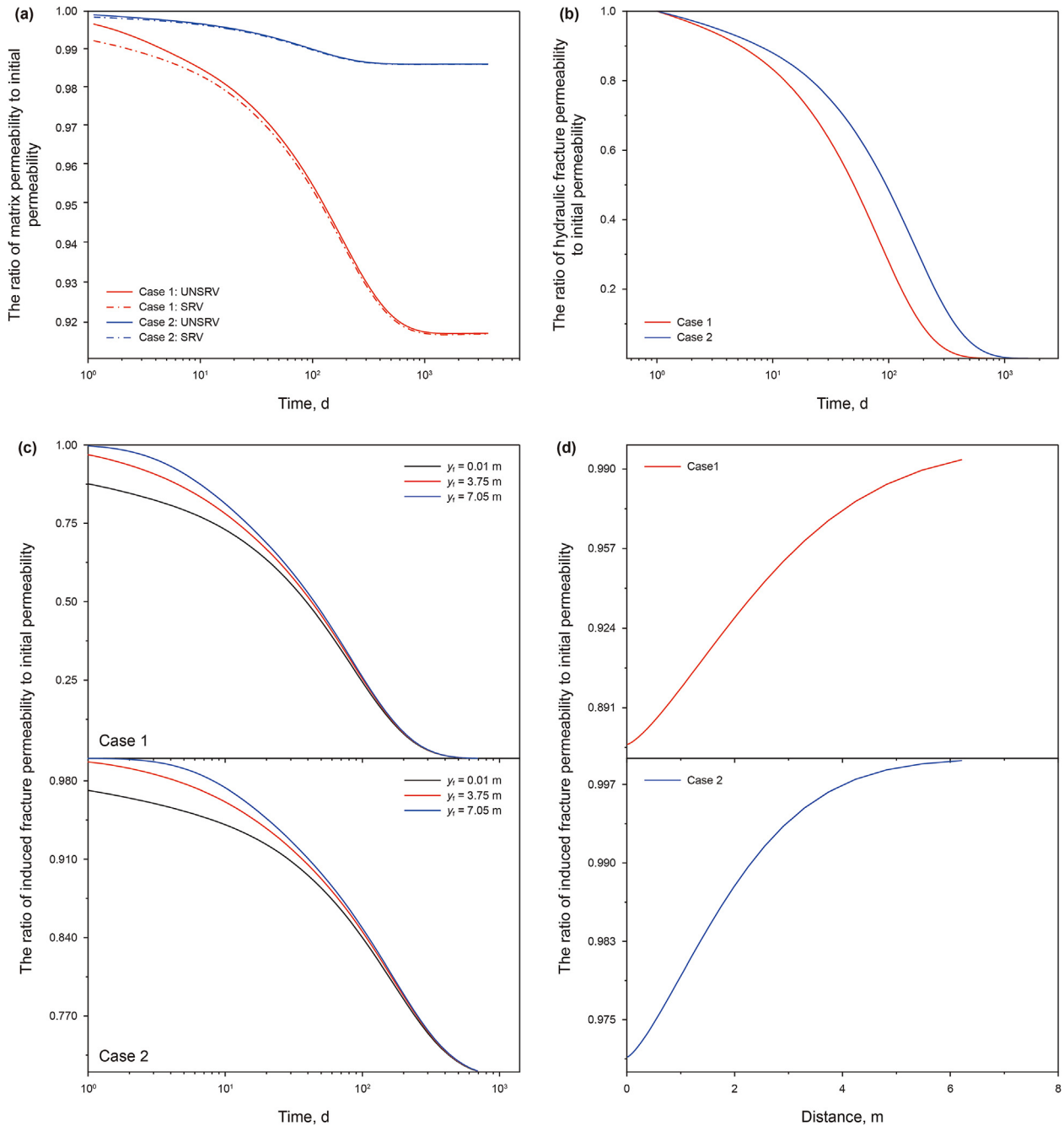

Fig. 7. The ratio of permeability in different media. Permeability ratio of matrix (**a**), hydraulic fracture (**b**), and induced fracture (**c**) with time; (**d**) Permeability ratio of induced fracture with distance (t = 1 d).

fractures in case 1, however, is greater than that of case 2, and the matrix compressibility in case 1 is lower than that in case 2. The main flow channels are induced fractures and hydraulic fractures, which are highly stress-sensitive. Fractures will close as the reservoir pressure decreases, preventing pressure propagation and production. At the same time, the matrix, as the main reservoir space, has low elastic energy, which is not conducive to oil production.

Fig. 8(a) shows that in case 2, the variation of interporosity flow coefficient is clearly smaller than in case 1. Fig. 8(b) shows if the matrix and induced fractures are not stress-sensitive, the interporosity flow coefficient is clearly larger than in the two cases where stress-sensitivity exists, and the interporosity flow coefficient in case 1 is significantly smaller than that in case 2. Across both cases, the interporosity flow coefficient decreases at a significant rate near the hydraulic fracture, while the variation range of interporosity flow coefficient decreases with distance.

The induced fractures are distributed fractally. As the induced fractures become closer to the hydraulic fracture, the more developed fracture network makes it easier for oil in the matrix flow into the fractures. A larger fracture spacing causes a decrease in interporosity flow capacity, resulting in a smaller interporosity flow coefficient.

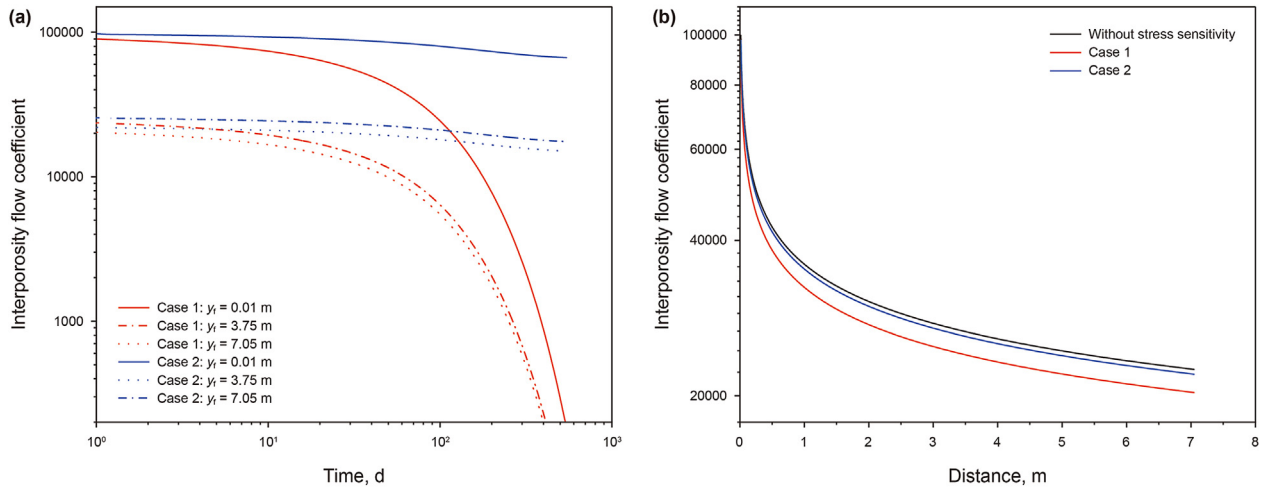

Fig. 8. Interporosity flow coefficient in SRV. (**a**) Interporosity flow coefficient versus time; (**b**) Interporosity flow coefficient versus distance (t = 1 d).

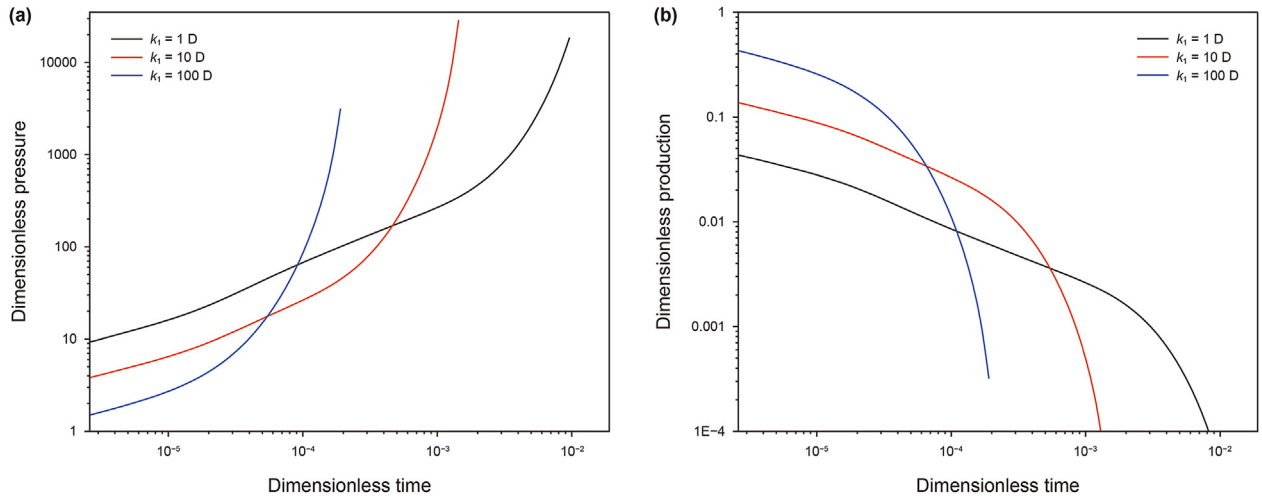

Fig. 9. The influence of hydraulic fracture conductivity on dimensionless pressure (**a**) and production (**b**).

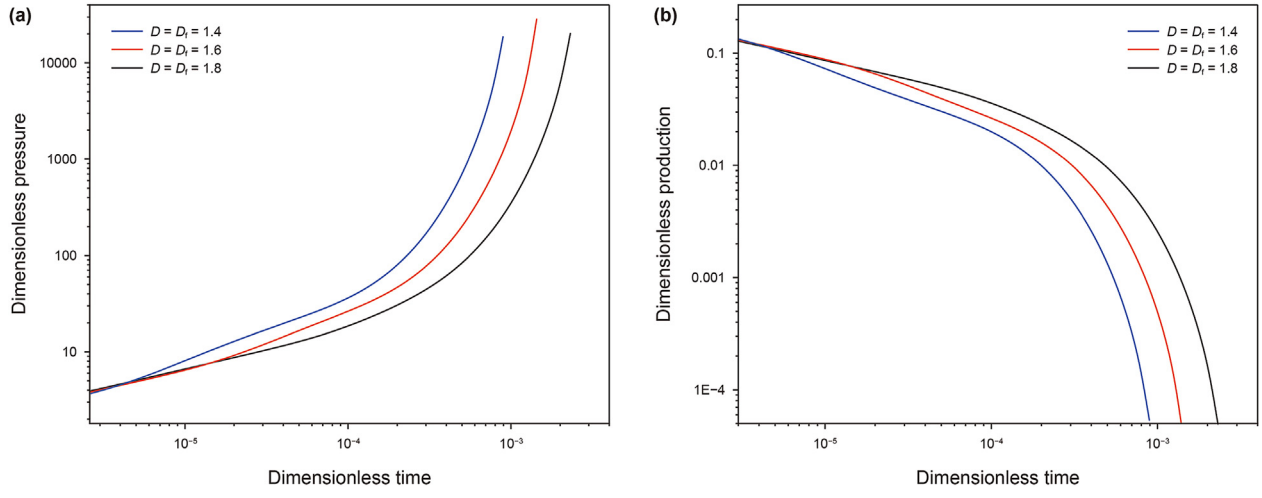

Fig. 10. The influence of fractal dimension of induced fractures on dimensionless pressure (**a**) and production (**b**).

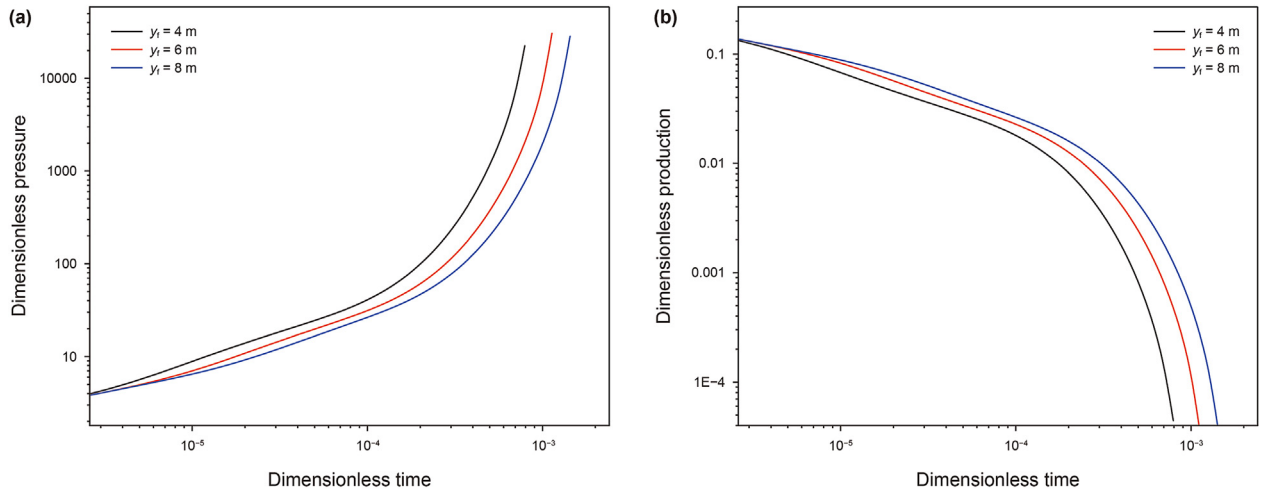

Fig. 11. The influence of SRV half width on dimensionless pressure (**a**) and dimensionless production (**b**).

3.3. Sensitivity analysis

This section analyzes the sensitivity of key parameters for hydraulic fracture and SRV. It is based on the stress sensitive coefficient and compressibility of case 2 in the previous section.

3.3.1. Conductivity of hydraulic fracture

Pressure and production are significantly affected by hydraulic fracture conductivity, as shown in Fig. 9.

As can be seen from Fig. 9(a) when the conductivity of hydraulic fractures is low, the early dimensionless pressure is large. However, reservoirs with low hydraulic fracture conductivity exhibit smaller dimensionless pressure at the later stage of production. In Fig. 9(b), it can be seen that the early oil flow rate is slow when hydraulic fractures have a low conductivity, and the oil flow rate at the later stage is gradually greater than that of reservoirs with high conductivity of hydraulic fractures.

The early oil flow capacity is strong in reservoirs with large hydraulic fracture conductivity, which leads to a rapid decrease in reservoir pressure, resulting in the loss of permeability both of the induced fractures and the matrix. Moreover, the matrix permeability is small, and the oil supply rate is much smaller than the production rate, so the later production will decline rapidly.

3.3.2. Fractal dimension of induced fractures

Oil flows horizontally in this model without vertical flow. In two-dimensional space, fractal dimension is 1 to 2. Large fractal dimension indicates better porosity and permeability, as well as denser fractures. Fig. 10 illustrates the influence of fractal dimension on pressure and production.

As can be seen in Fig. 10(a) and (b), the dimensionless pressure is smaller and the dimensionless production is much higher when the fractal dimension is large. The induced fracture spacing is determined by the fractal dimension. The SRV with small spacing has more flow channels, making them more conducive to production.

3.3.3. Half width of SRV

The half width of SRV represents the effective hydraulic fracturing range. With increasing SRV half width, production benefits as well. The effect on pressure and production can be seen in Fig. 11.

Fig. 11(a) illustrates that as the SRV half width decreases, the dimensionless pressure increases. Additionally, during the early stages, the pressure difference among different half width is relatively small. Increasing the SRV half width from 4 to 6 m, the reduction in pressure is significantly greater than by increasing the SRV half width from 6 to 8 m. It can be seen from Fig. 11(b) that the greater the SRV half width, the larger the production in the middle stages, and the greater the impact on this stage of production.

A large SRV half width, that is, a large effective SRV, will result in a wider fracture network, expanding shale oil flow channels, which will lead to higher production.

4. Conclusions

In this paper, a multi-scale coupled flow mathematical model considering the stress sensitive characteristics of multi-scale media is proposed, which fully combines the fractal characteristics of nanopores and induced fractures after fracturing to more accurately characterize shale oil flow and realize rapid productivity evaluation. The accuracy of the model is verified by numerical solution and production data from actual field. The pressure, production, permeability loss of different media and interporosity flow coefficient in different stress-sensitive reservoirs are analyzed. Finally, the stress sensitivity analysis is carried out. The main conclusions are as follows:

(1) The numerical solution is used to verify the accuracy of the model, but it is also worthwhile mentioning that the model can significantly shorten calculation time and enable rapid evaluation of productivity.
(2) Induced fractures exhibit low stress sensitivity when proppant provides strong support to them, and their permeability loss is about 30%. High stress sensitivity will inhibit interporosity flow from the matrix to fractures, which will have a significant negative impact on shale oil production.
(3) Sensitivity analysis shows that higher conductivity of hydraulic fractures benefits initial production, and the effect of fracturing will have a decisive impact on production.

Declaration of competing interest

The authors declare that there are no competing interests.

Acknowledgment

This study was supported by the National Natural Science Foundation of China (U22B2075, 52274056, 51974356).

Appendix A

Permeability and porosity of organic/inorganic matrix considering stress sensitivity, and those of organic matrix are as follows:

$$\phi_{om} = \phi_{om,i} e^{-C_m(p_i - p_m)}, \tag{A1}$$

$$k_{om} = k_{om,i} e^{-\gamma_m(p_i - p_m)}. \tag{A2}$$

Similarly, the permeability and porosity of inorganic pores can be obtained

$$\phi_{im} = \phi_{im,i} e^{-C_m(p_i - p_m)}, \tag{A3}$$

$$k_{im} = k_{im,i} e^{-\gamma_m(p_i - p_m)}. \tag{A4}$$

The permeability of organic pores can be calculated using HP equation:

$$k_{om,i} = \frac{\phi_{om,i} R_{om,i}^2}{8\tau_{om,i}}, \tag{A5}$$

$$k_{om} = \frac{\phi_{om} R_{om}^2}{8\tau_{om}}. \tag{A6}$$

Additionally, the permeability and porosity of inorganic pores are determined

$$k_{im,i} = \frac{\phi_{im,i} R_{im,i}^2}{8\tau_{im,i}}, \tag{A7}$$

$$k_{im} = \frac{\phi_{im} R_{im}^2}{8\tau_{im}}. \tag{A8}$$

The relationship between tortuosity and nanopore size in shale is as follows:

$$\tau_{im} = (2R_{im})^{1-D_\tau} L_s^{D_\tau - 1}. \tag{A9}$$

By combining Eqs. (A1), (A2), (A5) and (A6), we can determine the pore radius of organic matter,

$$R_{om} = R_{om,i} e^{\frac{1}{D_\tau + 1}(C_m - \gamma_m)(p_i - p_m)}. \tag{A10}$$

Inorganic pore radius can also be calculated using the Eqs. (A3), (A4), and (A7)–(A9):

$$R_{im} = R_{im,i} e^{\frac{1}{D_\tau + 1}(C_m - \gamma_m)(p_i - p_m)}. \tag{A11}$$

The velocity of near wall oil (Eq. (A12)) and bulk oil (Eq. (A13)) in an inorganic nanopore is expressed as follows (Zhang et al., 2017):

$$v_{nw}(r) = \frac{\partial p_m}{\partial x} \frac{R_{im}^2 - r^2}{4\mu_{im}} + C_1 \quad (R_{im} - \delta_{im} < r < R_{im}), \tag{A12}$$

$$v_b(r) = \frac{\partial p_m}{\partial x} \frac{R_{im}^2 - r^2}{4\mu_m} + C_2 \quad (0 < r < R_{im} - \delta_{im}). \tag{A13}$$

Using the continuous velocity and the slip boundary, the internal and external boundary conditions can be obtained as follows:

$$\begin{cases} \left.\dfrac{\partial v_b}{\partial r}\right|_{r=0} = 0 \\ -\lambda_{im} \left.\dfrac{\partial v_{nw}}{\partial r}\right|_{r=0} = v_{nw}|_{r=R_{im}} \\ v_{nw}|_{r=R_{im}-\delta_{im}} = v_b|_{r=R_{im}-\delta_{im}} \end{cases}.$$

By solving the flow equations subject to the boundary condition, velocity profiles of bulk and near-well oil transport in the inorganic nanopore are described in Eqs. (A14) and (A15), respectively:

$$v_b(r) = \left(\frac{R_{im}^2 - \frac{\mu_{im}}{\mu_m} r^2}{4\mu_{im}} - \frac{(\mu_m - \mu_{im})(R_{im} - \delta_{im})^2}{4\mu_m \mu_{im}} + \lambda_{im} \frac{R_{im}}{2\mu_{im}} \right) \frac{\partial p_m}{\partial x}. \tag{A14}$$

$$v_{nw}(r) = \left(\frac{R_{im}^2 - r^2}{4\mu_{im}} + \lambda_{im} \frac{R_{im}}{2\mu_{im}} \right) \frac{\partial p_m}{\partial x}. \tag{A15}$$

Appendix B

The dimensionless variables are defined as:

$$p_D = \frac{p_i - p_n}{p_i - p_{wf}}, \tag{B1}$$

$$x_D = \frac{x}{x_f}, \tag{B2}$$

$$y_D = \frac{y}{x_f}, \tag{B3}$$

$$y'_D = \frac{y'}{s_{fi}(y)}, \tag{B4}$$

$$t_D = \frac{k_w t}{(\phi C_t)_m \mu x_f^2}, \tag{B5}$$

$$a_{iD} = a_i \left(p_i - p_{wf} \right), \tag{B6}$$

$$q_D = \frac{\mu B}{k_w h \left(p_i - p_{wf} \right)} q. \tag{B7}$$

Pedrosa transform and Perturbation transform are described as follows:

$$p_{mD} = -\frac{1}{\chi_{mD}} \ln(1 - \chi_{mD} \xi_{mD}), \tag{B8}$$

$$\frac{1}{1 - \chi_{mD} \xi_{mD}} = 1 + \chi_{mD} \xi_{mD} + \chi_{mD}^2 \xi_{mD}^2 + \cdots, \tag{B9}$$

$$p_{fD} = -\frac{1}{\gamma_{fD}} \ln\left(1 - \gamma_{fD} \xi_{fD}\right), \tag{B10}$$

$$\frac{1}{1 - \gamma_{fD} \xi_{fD}} = 1 + \gamma_{fD} \xi_{fD} + \gamma_{fD}^2 \xi_{fD}^2 + \cdots. \tag{B11}$$

Appendix C

The solution of the governing equation in the SRV is as follows:

$$B_j = \frac{b_j^+ + b_j^-}{2w_{fD}^\theta}, \tag{C1}$$

$$I_j(y_D)=I_{\frac{1-h}{2+g-h}}\left(\frac{2\sqrt{B_j}}{2+g-h}y_D^{\frac{2+g-h}{2}}\right), \tag{C2}$$

$$I_j'(y_D)=I_{\frac{-1-g}{2+g-h}}\left(\frac{2\sqrt{B_j}}{2+g-h}y_D^{\frac{2+g-h}{2}}\right), \tag{C3}$$

$$K_j(y_D)=K_{\frac{1-h}{2+g-h}}\left(\frac{2\sqrt{B_j}}{2+g-h}y_D^{\frac{2+g-h}{2}}\right), \tag{C4}$$

$$K_j'(y_D)=K_{\frac{-1-g}{2+g-h}}\left(\frac{2\sqrt{B_j}}{2+g-h}y_D^{\frac{2+g-h}{2}}\right). \tag{C5}$$

$$\overline{\xi_{fDj}}=\overline{\xi_{fDj}}^{-'}\left(\frac{y_D^{(1-h)/2}}{\sqrt{B_j}\left(y_{jD}^-\right)^{(1+g-2h)/2}}\frac{I_j(y_D)K_j'\left(y_{jD}^+\right)+I_j'\left(y_{jD}^+\right)K_j(y_D)}{I_j'\left(y_{jD}^-\right)K_j'\left(y_{jD}^+\right)-I_j'\left(y_{jD}^+\right)K_j'\left(y_{jD}^-\right)}\right) -\overline{\xi_{fDj}}^{+'}\left(\frac{y_D^{(1-h)/2}}{\sqrt{B_j}\left(y_{jD}^+\right)^{(1+g-2h)/2}}\frac{I_j(y_D)K_j'\left(y_{jD}^-\right)+I_j'\left(y_{jD}^-\right)K_j(y_D)}{I_j'\left(y_{jD}^-\right)K_j'\left(y_{jD}^+\right)-I_j'\left(y_{jD}^+\right)K_j'\left(y_{jD}^-\right)}\right), \tag{C6}$$

$$\begin{aligned}\overline{\xi_{fDj}}^{-'}&\left(\frac{\left(y_{jD}^+\right)^{(1-h)/2}}{\sqrt{B_j}\left(y_{jD}^-\right)^{(1+g-2h)/2}}\frac{I_j\left(y_{jD}^+\right)K_j'\left(y_{jD}^+\right)+I_j'\left(y_{jD}^+\right)K_j\left(y_{jD}^+\right)}{I_j'\left(y_{jD}^-\right)K_j'\left(y_{jD}^+\right)-I_j'\left(y_{jD}^+\right)K_j'\left(y_{jD}^-\right)}\right)+\overline{\xi_{fDj}}^{+'}\left(-\frac{\left(y_{jD}^+\right)^{(1-h)/2}}{\sqrt{B_j}\left(y_{jD}^+\right)^{(1+g-2h)/2}}\frac{I_j\left(y_{jD}^+\right)K_j'\left(y_{jD}^-\right)+I_j'\left(y_{jD}^-\right)K_j\left(y_{jD}^+\right)}{I_j'\left(y_{jD}^-\right)K_j'\left(y_{jD}^+\right)-I_j'\left(y_{jD}^+\right)K_j'\left(y_{jD}^-\right)}\right.\\ &\left.-\frac{\left(y_{(j+1)D}^-\right)^{(1-h)/2}}{\sqrt{B_j}\left(y_{(j+1)D}^-\right)^{(1+g-2h)/2}}\frac{I_{j+1}\left(y_{jD}^-\right)K_{j+1}'\left(y_{(j+1)D}^+\right)+I_{j+1}'\left(y_{(j+1)D}^+\right)K_{(j+1)}\left(y_{(j+1)D}^-\right)}{I_{j+1}'\left(y_{jD}^-\right)K_{j+1}'\left(y_{(j+1)D}^+\right)-I_{j+1}'\left(y_{(j+1)D}^+\right)K_{(j+1)}'\left(y_{(j+1)D}^-\right)}\right)\\ &+\overline{\xi_{fD(j+1)}}^{-'}\left(\frac{\left(y_{(j+1)D}^-\right)^{(1-h)/2}}{\sqrt{B_j}\left(y_{(j+1)D}^+\right)^{(1+g-2h)/2}}\frac{I_{j+1}\left(y_{(j+1)D}^-\right)K_{j+1}'\left(y_{(j+1)D}^-\right)+I_{j+1}'\left(y_{(j+1)D}^-\right)K_{j+1}\left(y_{(j+1)D}^-\right)}{I_{j+1}'\left(y_{(j+1)D}^-\right)K_{j+1}'\left(y_{(j+1)D}^+\right)-I_{j+1}'\left(y_{jD}^+\right)K_{j+1}'\left(y_{(j+1)D}^-\right)}\right)=0.\end{aligned} \tag{C7}$$

An equal pressure exists at the interface between the hydraulic fracture and induced fractures:

$$\overline{\xi_{fD1}}=\overline{\xi_{1D}}. \tag{C8}$$

The coefficient matrix can be obtained with boundary condition

$$D_1=\frac{\left(y_{1D}^-\right)^{(1-h)/2}}{\sqrt{B_1}\left(y_{1D}^-\right)^{(1+g-2h)/2}}\frac{I_1\left(y_{1D}^-\right)K_1'\left(y_{1D}^+\right)+I_1'\left(y_{1D}^+\right)K_1\left(y_{1D}^-\right)}{I_1'\left(y_{1D}^-\right)K_1'\left(y_{1D}^+\right)-I_1'\left(y_{1D}^+\right)K_1'\left(y_{1D}^-\right)}, \tag{C9}$$

$$D_2=\frac{\left(y_{1D}^+\right)^{(1-h)/2}}{\sqrt{B_1}\left(y_{1D}^+\right)^{(1+g-2h)/2}}\frac{I_1\left(y_{1D}^+\right)K_1'\left(y_{1D}^-\right)+I_1'\left(y_{1D}^-\right)K_1\left(y_{1D}^+\right)}{I_1'\left(y_{1D}^-\right)K_1'\left(y_{1D}^+\right)-I_1'\left(y_{1D}^+\right)K_1'\left(y_{1D}^-\right)}, \tag{C10}$$

$$C_{j,j-1}=\frac{\left(y_{jD}^+\right)^{(1-h)/2}}{\sqrt{B_j}\left(y_{jD}^-\right)^{(1+g-2h)/2}}\frac{I_j\left(y_{(j+1)D}^+\right)K_j'\left(y_{jD}^+\right)+I_j'\left(y_{jD}^+\right)K_j\left(y_{jD}^+\right)}{I_j'\left(y_{jD}^-\right)K_j'\left(y_{jD}^+\right)-I_j'\left(y_{jD}^+\right)K_j'\left(y_{jD}^-\right)}, \tag{C11}$$

$$\begin{aligned}C_{j,j}=&-\frac{\left(y_{jD}^+\right)^{(1-h)/2}}{\sqrt{B_j}\left(y_{jD}^+\right)^{(1+g-2h)/2}}\frac{I_j\left(y_{jD}^+\right)K_j'\left(y_{jD}^-\right)+I_j'\left(y_{jD}^-\right)K_j\left(y_{jD}^+\right)}{I_j'\left(y_{jD}^-\right)K_j'\left(y_{jD}^+\right)-I_j'\left(y_{jD}^+\right)K_j'\left(y_{jD}^-\right)}\\ &-\frac{\left(y_{(j+1)D}^-\right)^{(1-h)/2}}{\sqrt{B_j}\left(y_{(j+1)D}^-\right)^{(1+g-2h)/2}}\frac{I_{j+1}\left(y_{(j+1)D}^-\right)K_{j+1}'\left(y_{(j+1)D}^+\right)+I_{j+1}'\left(y_{(j+1)D}^+\right)K_{j+1}\left(y_{(j+1)D}^-\right)}{I_{j+1}'\left(y_{(j+1)D}^-\right)K_{j+1}'\left(y_{(j+1)D}^+\right)-I_{j+1}'\left(y_{(j+1)D}^+\right)K_{j+1}'\left(y_{(j+1)D}^-\right)},\end{aligned} \tag{C12}$$

$$C_{jj+1}=\frac{\left(y_{(j+1)\mathrm{D}}^{-}\right)^{(1-h)/2}}{\sqrt{B_{j+1}}\left(y_{(j+1)\mathrm{D}}^{+}\right)^{(1+g-2h)/2}}\frac{I_{j+1}\left(y_{(j+1)\mathrm{D}}^{-}\right)K'_{j+1}\left(y_{(j+1)\mathrm{D}}^{-}\right)+I'_{j+1}\left(y_{(j+1)\mathrm{D}}^{-}\right)K_{j+1}\left(y_{(j+1)\mathrm{D}}^{-}\right)}{I'_{j+1}\left(y_{(j+1)\mathrm{D}}^{-}\right)K'_{j+1}\left(y_{(j+1)\mathrm{D}}^{+}\right)-I'_{j+1}\left(y_{(j+1)\mathrm{D}}^{+}\right)K'_{j+1}\left(y_{(j+1)\mathrm{D}}^{-}\right)}, \tag{C13}$$

$$\overline{\xi_{\mathrm{fD}}}=y_{\mathrm{D}}^{\frac{1-h}{2}}\left[AI_{\frac{1-h}{2+g-h}}\left(\frac{2\sqrt{s}}{2+g-h}y_{\mathrm{D}}^{\frac{2+g-h}{2}}\right)+BK_{\frac{1-h}{2+g-h}}\left(\frac{2\sqrt{s}}{2+g-h}y_{\mathrm{D}}^{\frac{2+g-h}{2}}\right)\right]. \tag{C14}$$

References

Al-Obaidy, R.T., Gringarten, A.C., Sovetkin, V., 2014. Modeling of induced hydraulically fractured wells in shale reservoirs using 'branched' fractals. In: SPE Annual Technical Conference and Exhibition. https://doi.org/10.2118/170822-MS.

Bernabe, Y., 1986. The effective pressure law for permeability in Chelmsford granite and Barre granite. Int. J. Rock Mech. Min. Sci. Geomech. Abstracts. https://doi.org/10.1016/0148-9062(86)90972-1.

Bustin, R.M., Bustin, A.M., Cui, X., Ross, D.J.K., Pathi, V.M., 2008. Impact of shale properties on pore structure and storage characteristics. In: SPE Shale Gas Production Conference. https://doi.org/10.2118/119892-MS.

Cai, J., Zhang, Z., Wei, W., Guo, D., Li, S., Zhao, P., 2019. The critical factors for permeability-formation factor relation in reservoir rocks: pore-throat ratio, tortuosity and connectivity. Energy 188, 116051. https://doi.org/10.1016/j.energy.2019.116051.

Chen, D., Pan, Z., Ye, Z., 2015. Dependence of gas shale fracture permeability on effective stress and reservoir pressure: model match and insights. Fuel 139, 383–392. https://doi.org/10.1016/j.fuel.2014.09.018.

Chhatre, S.S., Sinha, S., Esch, W.L., Determan, M.D., Passey, Q.R., Leonardi, S.A., Braun, E.M., 2014. Effect of stress, creep, and fluid type on steady state permeability measurements in tight liquid unconventional reservoirs. In: Unconventional Resources Technology Conference. https://doi.org/10.15530/urtec-2014-1922578.

Cui, J., Sang, Q., Li, Y., Yin, C., Li, Y., Dong, M., 2017. Liquid permeability of organic nanopores in shale: calculation and analysis. Fuel 202, 426–434. https://doi.org/10.1016/j.fuel.2017.04.057.

Ding, D.Y., 2019. Modeling of matrix/fracture transfer with nonuniform-block distributions in low-permeability fractured reservoirs. SPE J. 24 (6), 2653–2670. https://doi.org/10.2118/191811-PA.

Fan, D., Ettehadtavakkol, A., 2017. Semi-analytical modeling of shale gas flow through fractal induced fracture networks with microseismic data. Fuel 193, 444–459. https://doi.org/10.1016/j.fuel.2016.12.059.

Feng, Q., Xu, S., Wang, S., Li, Y., Gao, F., Xu, Y., 2019. Apparent permeability model for shale oil with multiple mechanisms. J. Petrol. Sci. Eng. 175, 814–827. https://doi.org/10.1016/j.petrol.2019.01.038.

Gonzalez, L., Nasreldin, G., Rivero, J., Welsh, P., Aguilera, R., 2014. 3D modeling of multistage hydraulic fractures and two-way-coupling geomechanics/fluid-flow simulation of a horizontal well in the nikanassin tight gas formation, Western Canada sedimentary basin. SPE Reservoir Eval. Eng. 17 (2), 257–270. https://doi.org/10.2118/159765-PA.

Guo, T., Tang, S., Liu, S., Liu, X., Xu, J., Qi, N., Rui, Z., 2021. Physical simulation of hydraulic fracturing of large-sized tight sandstone outcrops. SPE J. 26 (1), 372–393. https://doi.org/10.2118/204210-PA.

Gutierrez, M., Katsuki, D., Tutuncu, A., 2015. Determination of the continuous stress-dependent permeability, compressibility and poroelasticity of shale. Mar. Petrol. Geol. 68, 614–628. https://doi.org/10.1016/j.marpetgeo.2014.12.002.

Hu, B., Wang, J., Ma, Z., Sang, S., 2021. Permeability and thermal conductivity models of shale matrix with a bundle of tortuous fractal tree-like branching micropore networks. Int. J. Therm. Sci. 164, 106876. https://doi.org/10.1016/j.ijthermalsci.2021.106876.

Katende, A., Rutqvist, J., Massion, C., Radonjic, M., 2023. Experimental flow-through a single fracture with monolayer proppant at reservoir conditions: a case study on Caney Shale, Southwest Oklahoma, USA. Energy 273, 127181. https://doi.org/10.1016/j.energy.2023.127181.

Kazemi, H., 1969. Pressure transient analysis of naturally fractured reservoirs with uniform fracture distribution. SPE J. 9 (4), 451–462. https://doi.org/10.2118/2156-PA.

Lei, Z., Li, J., Chen, Z., Dai, X., Ji, D., Wang, Y., Liu, Y., 2023. Characterization of multiphase flow in shale oil reservoirs considering multiscale porous media by high-resolution numerical simulation. SPE J. 1–16. https://doi.org/10.2118/215847-PA.

Li, K., Zeng, F., Cai, J., Sheng, G., Xia, P., Zhang, K., 2018. Fractal characteristics of pores in Taiyuan formation shale from Hedong coal field, China. Fractals 26 (2), 1840006. https://doi.org/10.1142/S0218348X18400066.

Li, Y., Liu, X., Hu, Z., Duan, X.G., Chang, J., Zhou, G.Z., 2019. Research progress on fracture network simulation in shale reservoirs. Oil Geophys. Prospect. 54 (2), 480–492. https://doi.org/10.13810/j.cnki.issn.1000-7210.2019.02.028 (in Chinese).

Li, Z., Zou, Y.R., Xu, X.Y., Sun, J.N., Li, M., 2016. Adsorption of mudstone source rock for shale oil–Experiments, model and a case study. Org. Geochem. 92, 55–62. https://doi.org/10.1016/j.orggeochem.2015.12.009.

Luo, W., Tang, C., Feng, Y., Zhu, M., 2018. Mechanism of fluid flow along a dynamic conductivity fracture with pressure-dependent permeability under constant wellbore pressure. J. Petrol. Sci. Eng. 166, 465–475. https://doi.org/10.1016/j.petrol.2018.03.059.

Mattia, D., Calabrò, F., 2012. Explaining high flow rate of water in carbon nanotubes via solid–liquid molecular interactions. Microfluid. Nanofluidics 13, 125–130. https://doi.org/10.1007/s10404-012-0949-z.

Mei, L., Zhang, H., Wang, L., Zhang, Q., Cai, J., 2020. Fractal analysis of shape factor for matrix-fracture transfer function in fractured reservoirs. Oil & Gas Science and Technology–Revue d'IFP Energies nouvelles 75, 47. https://doi.org/10.2516/ogst/2020043.

Nandlal, K., Weijermars, R., 2019. Drained rock volume around hydraulic fractures in porous media: planar fractures versus fractal networks. Petrol. Sci. 16, 1064–1085. https://doi.org/10.1007/s12182-019-0333-7.

Pedrosa Jr., O.A., 1986. Pressure transient response in stress-sensitive formations. In: SPE Western Regional Meeting. https://doi.org/10.2118/15115-MS.

Qanbari, F., Clarkson, C.R., 2013. Analysis of transient linear flow in tight oil and gas reservoirs with stress-sensitive permeability and multi-phase flow. In: SPE Canada Unconventional Resources Conference. https://doi.org/10.2118/167176-MS.

Ren, Z., Wu, X., Han, G., Liu, L., Wu, X., Zhang, G., Lin, H., Zhang, J., Zhang, X., 2017. Transient pressure behavior of multi-stage fractured horizontal wells in stress-sensitive tight oil reservoirs. J. Petrol. Sci. Eng. 157, 1197–1208. https://doi.org/10.1016/j.petrol.2017.07.073.

Sheng, G., Javadpour, F., Su, Y., Liu, J., Li, K., Wang, W., 2019. A semianalytic solution for temporal pressure and production rate in a shale reservoir with nonuniform distribution of induced fractures. SPE J. 24 (4), 1856–1883. https://doi.org/10.2118/195576-PA.

Valdes-Perez, A., Blasingame, T.A., 2021. Pressure-transient behavior of double-porosity reservoirs with transient interporosity transfer with fractal matrix blocks. SPE J. 26 (4), 2417–2439. https://doi.org/10.2118/190841-PA.

Wang, Q., Wang, T., Liu, W., Zhang, J., Feng, Q., Lu, H., 2019. Relationships among composition, porosity and permeability of longmaxi shale reservoir in the weiyuan block, sichuan basin, China. Mar. Petrol. Geol. 102, 33–47. https://doi.org/10.1016/j.marpetgeo.2018.12.026.

Wang, S., Javadpour, F., Feng, Q., 2016. Molecular dynamics simulations of oil transport through inorganic nanopores in shale. Fuel 171, 74–86. https://doi.org/10.1016/j.fuel.2015.12.071.

Wang, W., Shahvali, M., Su, Y., 2015. A semi-analytical fractal model for production from tight oil reservoirs with hydraulically fractured horizontal wells. Fuel 158, 612–618. https://doi.org/10.1016/j.fuel.2015.06.008.

Wang, X., Li, J., Jiang, W., Zhang, H., Feng, Y., Yang, Z., 2022. Characteristics, current exploration practices, and prospects of continental shale oil in China. Advances in Geo-Energy Research 6 (6), 454–459. https://doi.org/10.46690/ager.2022.06.02.

Warren, J.E., Root, P.J., 1963. The behavior of naturally fractured reservoirs. SPE J. 3 (3), 245–255. https://doi.org/10.2118/426-PA.

Yan, X., Sun, J., Liu, D., 2019. Numerical simulation of shale gas multiscale seepage mechanism-coupled stress sensitivity. J. Chem. 2019, 1–13. https://doi.org/10.1155/2019/7387234.

Yang, D., Wang, W., Chen, W., Wang, S., Wang, X., 2017. Experimental investigation on the coupled effect of effective stress and gas slippage on the permeability of shale. Sci. Rep. 7 (1), 44696. https://doi.org/10.1038/srep44696.

Yang, D., Wang, W., Li, K., Chen, W., Yang, J., Wang, S., 2019. Experimental investigation on the stress sensitivity of permeability in naturally fractured shale. Environ. Earth Sci. 78, 1–10. https://doi.org/10.1007/s12665-019-8045-2.

Yao, J., Sun, H., Fan, D., Huang, Z., Sun, Z., Zhang, G., 2013. Transport mechanisms and numerical simulation of shale gas reservoirs. Journal of China University of Petroleum 37 (1), 91–98 (in Chinese).

Yu, B., Cheng, P., 2002. A fractal permeability model for bi-dispersed porous media. Int. J. Heat Mass Tran. 45 (14), 2983–2993. https://doi.org/10.1016/S0017-9310(02)00014-5.

Yu, H., Wang, Z., Rezaee, R., Zhang, Y., Han, T., Arif, M., Johnson, L., 2018. Porosity estimation in kerogen-bearing shale gas reservoirs. J. Nat. Gas Sci. Eng. 2, 575–581. https://doi.org/10.1016/j.jngse.2018.02.012.

Zeng, F., Zhang, Y., Guo, J., Ren, W., Jiang, Q., Xiang, J., 2020. Prediction of shale apparent liquid permeability based on fractal theory. Energy Fuels 34 (6), 6822–6833. https://doi.org/10.1021/acs.energyfuels.0c00318.

Zeng, J., Liu, J., Li, W., Leong, Y.K., Elsworth, D., Guo, J., 2021. Shale gas reservoir modeling and production evaluation considering complex gas transport mechanisms and dispersed distribution of kerogen. Petrol. Sci. 18, 195–218. https://doi.org/10.1007/s12182-020-00495-1.

Zhang, F., Emami-Meybodi, H., 2020. Flowback fracture closure of multi-fractured horizontal wells in shale gas reservoirs. J. Petrol. Sci. Eng. 186, 106711. https://doi.org/10.1016/j.petrol.2019.106711.

Zhang, F.Y., Zou, L.J., Rui, Z.H., Emami-Meybodi, H., Ayala, L.F., Zhang, Z.X., 2023. A two-phase type-curve method with multiscale fluid transport mechanisms in hydraulically fractured shale reservoirs. Petrol. Sci. 20 (4), 2253–2267. https://doi.org/10.1016/j.petsci.2023.02.004.

Zhang, Q., Su, Y., Wang, W., Lu, M., Sheng, G., 2017. Apparent permeability for liquid transport in nanopores of shale reservoirs: coupling flow enhancement and near wall flow. Int. J. Heat Mass Tran. 115, 224–234. https://doi.org/10.1016/j.ijheatmasstransfer.2017.08.024.

Zhang, T., Li, X., Shi, J., Sun, Z., Yin, Y., Wu, K., Feng, D., 2018. An apparent liquid permeability model of dual-wettability nanoporous media: a case study of shale. Chem. Eng. Sci. 187, 280–291. https://doi.org/10.1016/j.ces.2018.05.016.

Zhang, T., Li, X., Yin, Y., He, M., Liu, Q., Huang, L., Shi, J., 2019. The transport behaviors of oil in nanopores and nanoporous media of shale. Fuel 242, 305–315. https://doi.org/10.1016/j.fuel.2019.01.042.

Zheng, S., Manchanda, R., Sharma, M.M., 2020. Modeling fracture closure with proppant settling and embedment during shut-in and production. SPE Drill. Complet. 35 (4), 668–683. https://doi.org/10.2118/201205-PA.

Zhu, C., Sheng, J.J., Ettehadtavakkol, A., Li, Y., Dong, M., 2020. Numerical and experimental study of oil transfer in laminated shale. Int. J. Coal Geol. 217, 103365. https://doi.org/10.1016/j.coal.2019.103365.